ARTICLE

Inhibition of Lithium Dendrite Growth with Highly Concentrated Ions: Cellular Automaton Simulation and Surrogate Model with Ensemble Neural Networks†

Received 00th September 2021,
Accepted 00th January 2021

DOI: 10.1039/x0xx00000x

Tong Gao,[a] Ziwei Qian, [a] Hongbo Chen, [a,b] Reza Shahbazian-Yassar [c] and Issei Nakamura *[a]

We have developed a lattice Monte Carlo (MC) simulation based on the diffusion-limited aggregation model that accounts for the effect of the physical properties of small ions such as inorganic ions and large salt ions that mimic ionic liquids (ILs) on lithium dendrite growth. In our cellular automaton model, molecular and atomistic details are largely coarse-grained to reduce the number of model parameters. During lithium deposition, the cations of the salt and ILs form positively charged electrostatic shields around the tip of the dendrites, and the anions of the salt and ILs form negative local potential lumps in adjacent areas to the dendrite. Both of the effects change the distribution of the electrostatic potential and notably inhibit dendrite formation between electrodes. The applied voltage and the physical properties of the salt ions and ILs, such as the size of the ions, the size asymmetry between the cation and anion, the dielectric constant, the excluded volume of the ions, and the model parameter η, notably affect electric-field screening and hence the variation in the local potential, resulting in substantial changes in the aspect ratio and the average height of the dendrites. Our present results suggest that the large salts such as ILs more significantly inhibit the dendrite growth than the small ions, mainly because the ions highly dissociated in ILs can participate in electrostatic shielding to a greater degree. To reduce the computational complexity and burden of the MC simulation, we also constructed a surrogate model with ensemble neural networks.

I. Introduction

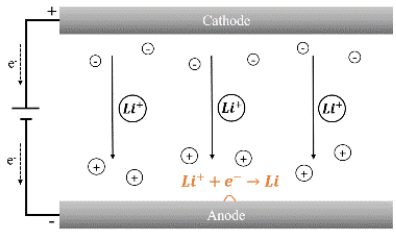

Fig. 1 Lithium metal electrodeposition during the charging process in a lithium-ion battery.

Lithium metal deposition is a phenomenon that occurs during the charging and discharging of lithium-ion batteries. As the battery is charged, lithium ions are released from the positive cathode, travel through electrolytes, and are intercalated into the graphene layers of the graphite (negative anode). During this charge phase, deposits solidified on the surface of the anode can form branching tree-like structures, the so-called lithium dendrite (Fig. 1). The growth trend of the deposits is spatially uneven. Typically, needle-shaped or dendritic lithium grows on the surface of the anode over many discharge-recharge cycles.[1, 2] If dendrites grow too long, some dendrites may fall off and no longer participate in the reaction, which brings irreversible capacity loss to the battery.[3-5] Additionally, the grown dendrite may pierce the separator between the cathode and anode, forming a short circuit and potentially causing a catastrophic fire.[5-7] To maintain the safety of lithium-ion batteries, it is essential to identify the critical factors that substantially affect the process of metal solidification in electrolytes. Specifically, a general treatment to inhibit the dendrite growth will not only help to improve the safety of Li-ion batteries but also give further insights into the electrodeposition process in the electrochemical industry.[8, 9] Nevertheless, this research objective remains challenging because (1) there exist a wide choice of system parameters, such as the size of ions, the size asymmetry between the ions in electrolytes, dielectric constant, and applied voltage, and (2) the reactions associated with the dendrite growth involve multiple length and time scales. This complexity also often complicates the computational modeling of the dendrite formation under various environments, and thus a reduction in the number of model parameters would also help in identifying the optimal design of the electrolyte systems.

Over the past few decades, many studies have aimed to improve the stability of the electrodes,[10-13] the qualities of electrolytes [4, 14-21] and separator materials,[22, 23] and the charging methods [24-26] of lithium-ion batteries. Numerous researchers have recently reported metal electrodepositions in ionic liquid

[a] Department of Physics, Michigan Technological University, Houghton, Michigan 49931, USA
[b] State Key Laboratory of Polymer Physics and Chemistry, Changchun Institute of Applied Chemistry, Chinese Academy of Science, Changchun, Jilin 130022, China
[c] Department of Mechanical and Industrial Engineering, University of Illinois at Chicago, Chicago, Illinois 60607, USA
* inakamur@mtu.edu
† Electronic Supplementary Information (ESI) available: Experimental observation of uniform lithium dendrite. See DOI: 10.1039/x0xx00000x

(IL)-containing electrolytes.[8, 15, 27-29] Among others, an experimental study by Pearson et al. [29] suggests that the ionic strength plays an important role in causing substantial differences in dendrite growth between ILs and conventional organic liquid electrolytes. For example, the number of the nuclei increases and the dendrite growth rate decreases as the ionic strength is increased. Moreover, ILs increase the electrolyte viscosity, thus retarding dendrite formation. Similarly, our experimental observation of lithium dendrite in a combination of 1M LiPF6 in EC/DMC electrolyte and 10% IL [BMIM][TFSI] also showed remarkably uniform, unconventional dendrite growth in Fig. S1†. Therefore, further theoretical investigation of the effect of the ionic strength on the inhibition of dendrite formation, particularly with the visualization of dendrite growth and electrostatic potential maps, would probably provide a deeper understanding of the inhibition mechanism of dendrite growth.

Dendrite growth involves various physical and chemical interactions that occur over multiple lengths and time scales[30]. Accordingly, various computational approaches, such as Monte Carlo (MC) simulations,[26, 31, 32] molecular dynamics (MD) simulations,[33] Brownian dynamics (BD) simulations,[26] and phase-field models,[34-49] have been developed. For example, Selis and Seminario performed classical MD simulations and investigated the relationship between charging methods and lithium dendrite formation in a nanobattery.[33] However, the time scale of the MD simulations is typically limited to the order of nanoseconds and cannot adequately account for the mechanism of mesoscopic or macroscopic metal dendrite growth associated with salt ions and ILs. BD simulations are also particle-based methods but can access longer time scales and larger length scales. Aryanfar et al. presented a novel coarse-grained MC model based on Brownian motions to explore the effect of electric current density on dendrite formation.[26] Nevertheless, BD typically assumes implicit solvents, is often inadequate to account for strong electrostatic correlations, and is normally well-defined for solid bodies with vast amounts of collisions due to surrounding molecules within the momentum relaxation time. Phase-field models are powerful tools to study the nucleation and dendrite growth that occur on relatively longer time scales and larger length scales.[34-49] Nevertheless, the model of the free energy often contains numerous adjustable parameters and may be constructed somewhat arbitrarily or empirically.[39] Thus, the development of more computationally tractable models with a relatively small number of model parameters that account for metal dendrite growth on the timescales beyond nanoseconds and the length scales beyond nanometers would also be convenient and beneficial from both the theoretical and experimental viewpoints.

Along the lines of a simulation method consisting of a minimal set of model parameters, Chen and Jorné developed a lattice simulation model for metal dendrite formation by considering zinc electrodeposition,[50] given that the diffusion-limited aggregation (DLA) model captures the pattern formation of the dendrite growth. This hypothesis is legitimate because the DLA model serves as an algorithm (or a cellular automaton [51, 52]) that simulates the solidification in which the microscopic reaction mechanisms are largely unknown and/or practically intractable. For example, the super-rough dynamics of tumor growth were discovered to exhibit the linear molecular beam epitaxy universality class,[53-55] a feature which can be simulated by the DLA (or Eden) model.[56] In the study by Chen and Jorné, the electrodeposition and morphology of zinc dendrites in a two-dimensional battery were observed. The fractal dimension determined by digitizing photographs was 1.7 and was consistent with the value 1.71 calculated by the simulations using the DLA model originally developed for a dielectric breakdown proposed by Niemeyer et al.[57] Thus, despite the drastic simplification of the coarse-grained lattice model, the agreement between theory and experiment is remarkable. Unfortunately, however, this lattice-simulation model has not been substantially developed over the past decades, and thus the application of the simulation model to salt-doped liquids and highly concentrated ions remains limited.

In this paper, we study the effect of small salt ions and large salt ions that mimic ILs on dendrite growth by considering the height and aspect ratio of the dendrite. We develop the DLA model on the lattice originally proposed by Niemeyer et al. to mimic lithium dendrite growth in electrolytes, mainly motivated by the model feasibility for zinc dendrite.[50] Moreover, it is well known that although the DLA model (or cellular automaton model) largely simplifies or ignores reaction mechanisms on atomistic and molecular scales, it often captures the macroscopic formation pattern of solidification. Likewise, our present cellular automaton model for electrodepositions does not contain many atomistic and molecular details regarding the reaction mechanism of the metal solidification, yet it provides a convenient tool to investigate how the electrostatic interactions affect dendrite formation with a minimal set of model parameters and thus to identify a possible mechanism for the dendrite inhibition caused by the small salt ions and ILs. Regarding the thermodynamic ensemble of ion configurations, we employ the lattice model of large ions with the excluded volume by Borukhov et al.[58] This lattice model accounts for the electrical double layer near charged surfaces. In this manuscript, we consider the dendrite growth to be limited to two-dimensional systems for computational simplicity.

Nevertheless, the generalization of the MC simulations with various model parameters and the achievement of good statistical convergence with a large number of samples are not easy tasks in general. Moreover, we are aware that like other simulation techniques for dendrite formation, the present lattice MC simulation model may still involve a limitation on the direct comparison between the simulation and experimental data because real systems are typically larger than the simulation length scale, and the entire description of the electrostatic nature on the nanoscales regarding the dendrite formation is often significantly challenging. Thus, we also need a generic, tractable method that provides the design principle of electrochemical devices for the dendrite inhibition in electrolytes. To this end, we also considered a surrogate model using ensemble neural networks (ENNs) in machine learning

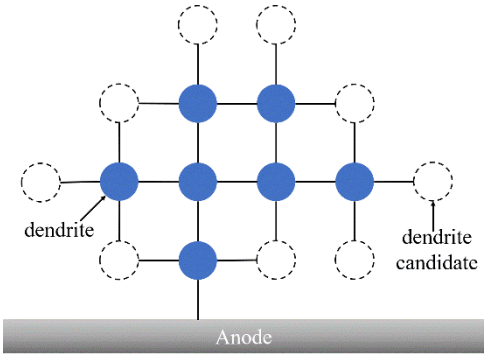

Fig. 2 2D schematic illustration of the lattice model. The blue circles describe the lithium dendrites, whereas the white circles describe dendrite candidates (or solvents) and salt ions, respectively.

techniques, as ENNs, or their variant, have proved to be useful tools that can outperform a single NN in various studies [59-63]. We show that our ENNs reasonably captures the non-monotonic trends of the MC simulation results, even though the number of simulation samples at each data point is decreased from the order of 200 to 20. Thus, our surrogate model serves as a convenient tool that enables fast characterization and design of the electrolytes with dendrite formation.

II. Model and Simulation Methods

Our lattice model based on the DLA algorithm consist of a cathode at the top, an anode at the bottom, and an electrolyte between them. The gist of the lattice DLA model includes the idea that when the reaction mechanism of microscopic events is intractable, the algorithm that solidification over the coarse-grained, mesoscopic length scales occurs at the lattice points is assumed. The validity of the model is often checked against bulk values such as the fractal dimension and the scaling law of the growth rate of solidification. Here, the molar concentration of the lithium ion in Li-ion batteries typically falls in the range of 0.1 to 1 [M]. In this case, the volume fractions of the lithium ion fall in the range of 0.00013 to 0.0013, and the molar concentrations are significantly smaller than those of other ionic species. For example, when the volume fraction of the added salt is 0.2, the ratio of the molar concentration of the lithium ion to that of the added salt falls in the range of 0.8 to 8 %. In other words, the contribution of the ionic strength of the lithium ion to those of the added salt is relatively insignificant. Thus, as an analog of the DLA model for the zinc dendrite formation[50], we treat the lithium ions dissolved in electrolytes as implicit (background) ions. The distance between each lattice point is 2 Å, and the lattice size is N×N, where N = 51. We fix the potentials of the anode (or dendrite) and cathode to 0 V and 0.5 V (unless otherwise noted), respectively. The periodic boundary condition is used in the direction parallel to the electrodes (see Fig. 1). Here, note that normal lithium-dendric branches typically grow over the micrometer scales. However, the repetition of significantly inhibited dendrite growth in ionic liquids shown in the subsequent section is likely to occur with increasing the system size, mainly because highly branching growths are considerably inhibited and do not appear beyond

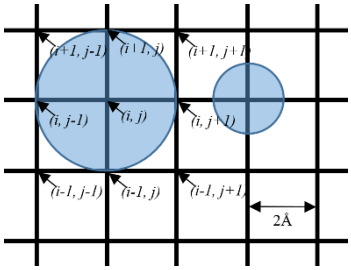

Fig. 3 Lattice occupancy of asymmetric particles in the lattice model.

one- or two-nanometer length scales in the present simulations. Such relatively homogeneous geometry would also be largely maintained in larger systems because the pattern formation in the DLA model exhibits fractal structure. Moreover, the Debye screening lengths ($\lesssim 1$ Å) in our simulations are significantly smaller than the system size. Thus, the system size is sufficiently large to consider the electrostatic correlations and the local growth mechanism of the dendrite. Nevertheless, the complete macroscopic pattern of the dendrite formation may also be further studied via other physical models such as the phase field model and Brownian dynamics simulation by accounting for the local growth mechanism derived from the present simulation model.

We illustrate our lattice system in Fig. 2. The blue circles represent the deposited lithium metals forming the lithium dendrite. The dendrite blobs stem from the negative electrode and thus have the same potential as that of the negative electrode. The white circles indicate the empty site for the candidate for the lithium dendrite in our MC method. Salt ions can also occupy those empty sites. The electric potential $\phi_{i,j}$ at the lattice point (i,j) consists of the electric potential $\phi_{i,j}^{E}$ produced by the electrodes and the Coulomb potential $\phi_{i,j}^{C}$ produced by the ions (treated as an explicit particle) as follows:

$$\phi_{i,j} = \phi_{i,j}^{E} + \phi_{i,j}^{C} \quad (1)$$

Note that the growth of the lithium dendrite indicates changes in the shape of the anode surface. Accordingly, the electrostatic field between the electrodes also changes due to the change in the boundary condition of the electrostatic potential on the anode. With these altered boundary conditions due to the geometric changes, we need to solve Laplace's equation [26]

$$\Delta^2 \phi^{E} = 0 \quad (2)$$

Here, we write Eq. (2) on the lattice in the following form [57]:

$$\phi_{i,j}^{E} = \frac{\left(\phi_{i+1,j}^{E} + \phi_{i-1,j}^{E} + \phi_{i,j+1}^{E} + \phi_{i,j-1}^{E}\right)}{4} \quad (3)$$

Here, $\phi_{i+1,j}^{E}$, $\phi_{i-1,j}^{E}$, $\phi_{i,j+1}^{E}$, and $\phi_{i,j-1}^{E}$ designate the electrostatic potentials of four neighboring lattice points around the (i,j) site. We note that the lattice model of Chen and Jorné included the effect of the electrical conductivity κ of water according to the modified Laplace equation, $\nabla \cdot [\kappa(\vec{r})\phi(\vec{r})] = 0$ [50]. However, the analysis of experimental data suggested that the electrical conductivity of water was about

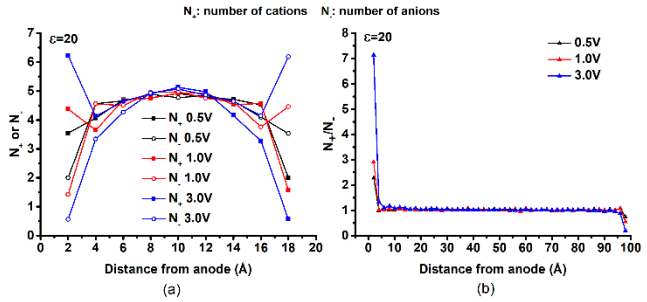

Fig. 4 Ion distributions from the electrodes for the dendrite-free simulation. The diameter of the cation (anion) is 2 Å. (a) Distance from the anode vs. the number N_+ (N_-) of the cations (anions). N=11 and the lattice occupancy of the ions is 76 %. (b) Distance from the anode vs. the ratio of N_+ to N_-. N=51 and the lattice occupancy of the ions is 60 %.

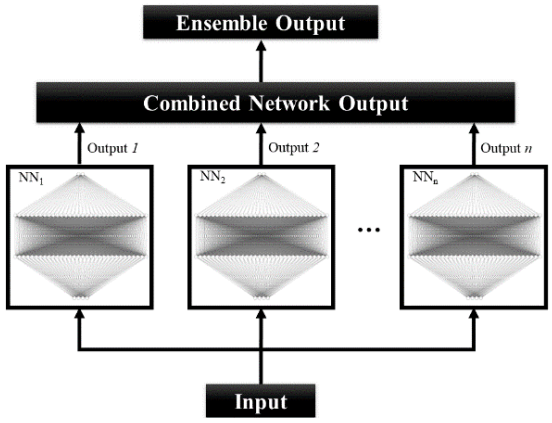

Fig. 5 ENN for the prediction of lithium dendrite growth. Each neuron contains an activation function.

1% of that of the dendrite, and the effect on the lattice model is insignificant. Given this situation, we do not consider the electrical conductivity κ in the present study. Concomitantly, this model simplification also enables us to explore the minimal effect to inhibit dendrite formation.

The Coulomb potential $\phi_{i,j}^{C}$ with the dielectric constant ε is given by

$$\phi_{i,j}^{C} = \frac{1}{4\pi\varepsilon_0\varepsilon}\sum_{k}\frac{q_k}{r_k} \quad (4)$$

where q_k is the k-th ionic charge and r_k is the distance between the lattice point (i,j) and the k-th ion. Fig. 3 illustrates the lattice occupancy of the ions with diameter d = 4 Å and d = 2 Å. The ions cannot be overlapped due to the effect of the excluded volume. A further remark about the treatment with the electrostatic interactions is discussed in the subsection, "A remark about the DLA model as a cellular automaton".

We perform the MC update according to the local potential $\phi_{i,j}$. This algorithm includes two update processes regarding the ion configuration and the dendrite growth. Our MC simulation causes the concentration gradient and the electric field gradient along the lines of the continuum theory for ion diffusion in Ref [64]. Here, we note that the computational cost of solving Eq. (2) for the trial configuration for the MC update by interaction is nominal because the solution is very close to the original potential (i.e., the initial guess). The DLA algorithm of the nucleation (or the pattern formation) at the lattice point (i,j) in Refs. [50] and [57] assumes the following heuristic growth probability:

$$p_{i,j} = \frac{(\phi_{i,j})^{\eta}}{\sum_{\langle i,j\rangle}(\phi_{i,j})^{\eta}} \quad (5)$$

Eq. (5) indicates the nucleation probability that the empty lattice point adjacent to the occupied lattice point is converted to the new dendrite point caused by the lithium deposition. The denominator represents the sum of the electrostatic potentials of all dendrite candidates (i.e., empty points adjacent to the occupied points). When $\phi_{i,j} \leq 0$, we set the probability to zero, assuming that the electron is unlikely to transfer from the electrode to the lithium ions in the negative potential area. The exponent η is the model parameter suggested by Niemeyer et al. [57] and associates the local potential with the nucleation probability. Experiments show that different metals have different values of the fractal dimension of the dendrites [65]. Thus, the exponent η can be determined by the fractal dimension observed in experiments. For example, η for the zinc dendrite may be fixed to reproduce the observed fractal dimension 1.7.[50] However, we are not aware of the fractal dimension of the lithium dendrite and therefore vary the values in the present study.

Here we write the total potential energies of the system before and after updating the positions of the ions as U_{old} and U_{new}, respectively. If the trial update decreases or does not change the potential energy, we accept the new state; otherwise, we accept the new state if a uniform random number becomes smaller than the Boltzmann distribution $e^{-\frac{(U_{new}-U_{old})}{kT}}$. The dendrite growth is significantly slower than the translational motion of the ions in the electrolytes. Accordingly, we consider the ratio of the trial update of the dendrite growth to that of the ion positions to be 1:500. It should also be noted that the present DLA algorithm is a clustering method to account for the fractal pattern of solidification and does not involve the explicit timescale of the deposition process.[50, 57]

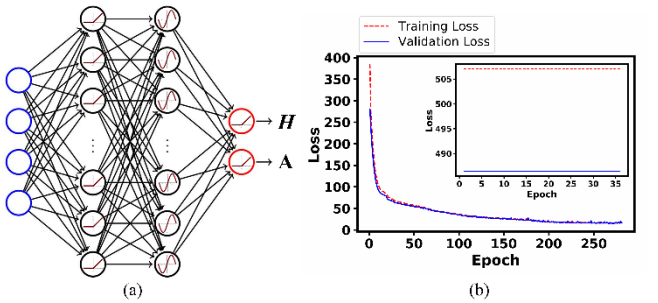

Fig. 6 Sub-NN system. (a) Architecture of our sub-NN with one input layer, two hidden layers, and one output layer, consisting of 4,32,32, and 2 neurons, respectively. The first hidden layer and the output layer include the ReLU activation function, whereas the activation function in the second hidden layer can be the sine function. (b) Sub-NNs' training loss and validation loss decrease with epochs during the training process. The inset shows an example of bad training.

To examine the model applicability for highly concentrated ions, we performed dendrite-free simulations with the dielectric constant ε =20 for small [Fig. 4 (a)] and large [Fig. 4

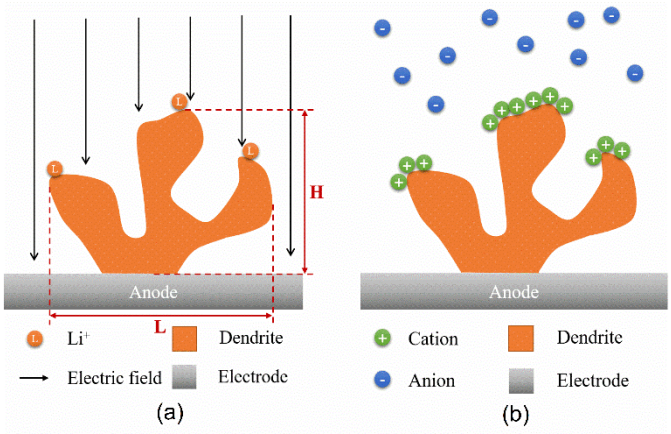

Fig. 7 Schematic illustration of lithium deposition: (a) Tip effect and (b) electrostatic shielding due to electric-field screening. Note that the actual electrostatic fields do not align parallel but are in highly anisotropic directions due to the dendrites.

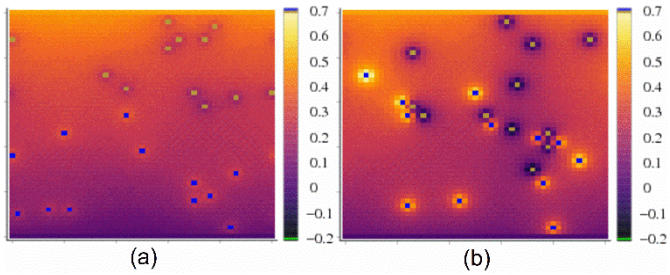

Fig. 8 Snapshot of the potential map for 1 % salts. The color bars indicate the potential difference from the anode potential. The brighter the color, the larger the potential. The dielectric constants of the electrolytes are (a) ε = 80 and (b) ε = 20. Blue and yellowish-green particles represent the cations and anions, respectively.

(b)] systems. Here, this dielectric constant compares favorably with the values of many common ILs and polar solvents. Overall, the results show the following two key features for large ions with excluded volume: the monolayer adsorption of the counterions near the electrodes and the recovery of the bulk density at a distance of a few monolayers from the electrodes. This fact is analogous to the results of the mean-field approximation [58] for ions with excluded volume and a molecular dynamics simulation [66] for ILs in a dielectric continuum.

A remark about the DLA model as a cellular automaton: The present lattice model is considered a cellular automaton, in which a minimal assigned rule on a regular grid of cells yields a qualitative feature of physical phenomena. Typically, cellular automata involve model parameters to reproduce a certain degree of complexity in targeted growth mechanisms [51, 52]. Here, note that our present treatment of the electrostatic interactions does not account for the effects of image charges (or induced surface charges) and the diffusion of the lithium ions near the dendrites, whereas these factors may also affect the dendrite growth. However, we assume that the electrostatic interactions due to these effects are electrically screened to a large degree by the highly concentrated ions, and thus the effects are relatively weaker. Therefore, we attribute the two effects to the model parameter η for our cellular automaton model, as the consistency between the present computational algorithm for implicit-metal ion models and the observed fractal dimension of zinc dendrites was demonstrated by Chen and Jorné [50].

Ensemble neural network: We employed 20 samples for each volume fraction to train our ENNs using Keras [67]. These samples are split into three parts: training, validation, and test datasets. As illustrated in Fig. 5, our ENN consists of an ensemble of 8 sub-NNs (Fig. 6) that have identical architecture with different activation functions. They are combined using linear regression. The topology of sub-NNs is 4-32-32-2, which represents the number of neurons in an input layer, the first hidden layer, the second hidden layer, and an output layer, respectively. We evaluated the model by the mean squared error (MSE) of the predicted value ($\hat{y}$) and the target value (y) (also referred to as a loss function) as follows:

$$\mathrm{MSE} = \frac{\sum(y - \hat{y})^2}{n} \qquad (6)$$

The neurons are fully connected between the neighboring layers, and each connection has a weight. The weights of all sub-NNs are randomly initialized and are optimized by minimizing the loss function. For the activation functions, we used ReLU, Gaussian, tanh, sigmoid, and trigonometric functions [Fig. 6(a)]. To reduce overfitting the model, we performed the early stopping of training with a patience setting of 20 epochs. Fig. 6(b) shows the training loss and validation loss of a well-trained sub-NN during the training process. The training and validation loss stop when the early stop condition is satisfied. We employed the dielectric constant (ε), model parameter (η), voltage (V), and volume fraction (ϕ) for the input variables and the average height (H) and aspect ratio (A) for the output layer.

III. Results and Analysis

In the subsequent subsections, we consider two cases as follows: (1) For symmetric ions, we set the grid size (2 Å) to the cation diameter d_+ and the anion diameter d_-. (2) For asymmetric ions, we consider (d_+, d_-) = (4 Å, 2 Å) and (2 Å, 4 Å). The amount of the salts is represented by the lattice occupancy that indicates the ratio of the number of the lattice sites occupied by the salt ions to the number of the total lattice sites. The objective of the present study is to examine how the dendrite surface grows with the salt ions. Thus, in addition to the calculation of the average height of the dendrite at a given MC step, we calculate the aspect ratio H/L of the dendrite to characterize the dendrite morphology, where H and L designate the height and width of dendrites, respectively (Fig. 7). For example, when the dendrite shape is relatively flat with a wider length and smaller height, the aspect ratio becomes small. We take a statistical average of 200 samples for each data point.

Mechanism of dendrite inhibition

Before we present each simulation result, we will discuss the primary mechanism that substantially suppresses the dendrite formation observed in our simulations. Note that a tip with a sharp edge on the metal electrode exhibits a stronger electrical field [68]. Thus, lithium ions tend to be deposited preferentially around the pointy regions of the dendrite, compared to

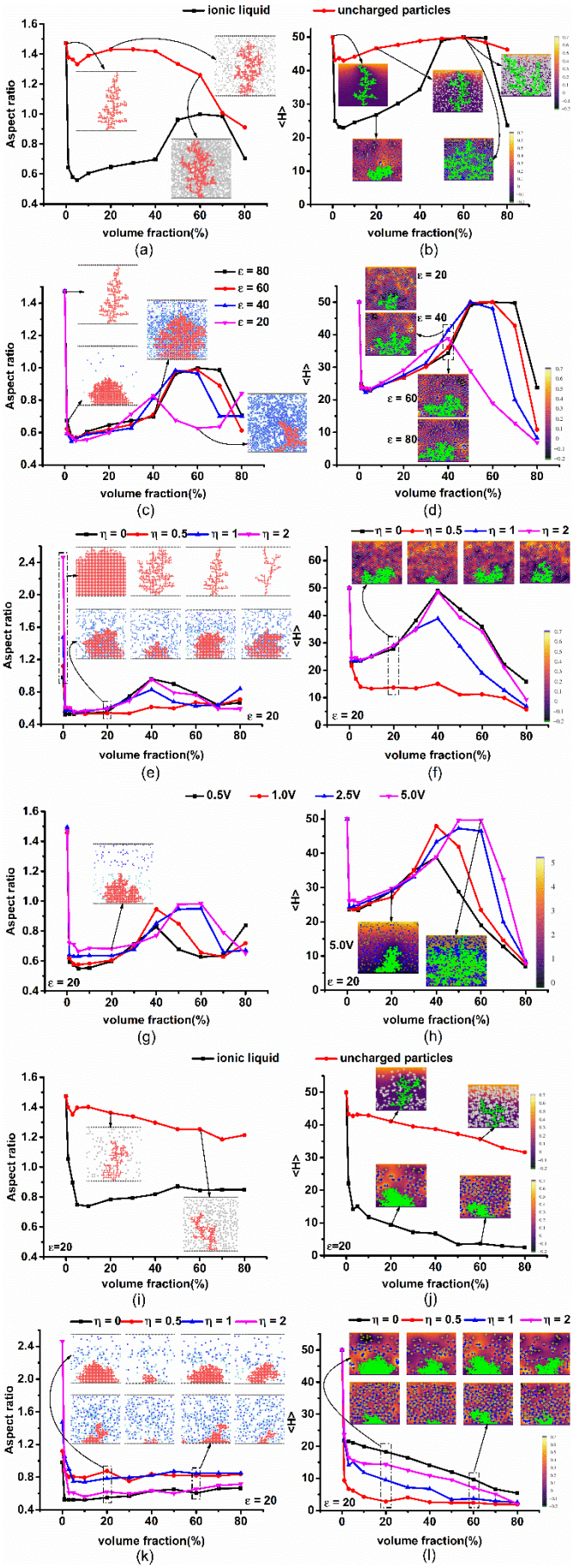

Fig. 9 Effects of the ionic charge, the dielectric constant, the parameter η, and the applied voltage on dendrite growth for the symmetric ions ($d_+ = d_-$). The x-axis is the lattice occupancy of the salts or uncharged particles. $\langle H \rangle$ designates the average height calculated after 2×10^7 MC steps. The applied voltage is 0.5 V in (a) – (f) and (i) – (l). The dielectric constants are ε = 80, unless otherwise noted. Insets in the figures in the left column: the anode (black), cathode (black), lithium dendrites (red), cations (light blue), anions (blue), and uncharged particles (silver). Insets on the right: lithium dendrites (green), cations (blue), anions (yellowish-green), and uncharged particles (silver).

rounded or smooth regions. This is referred to as "tip effect" (Fig. 7a). Accordingly, the dendrite solidification near the pointy regions tends to grow rapidly and form tree-like structures. However, when ILs are added, the cations tend to accumulate near the pointy regions of the dendrite, forming a layer of positive charges that cause electrostatic shielding (Fig. 7b). These positively charged layers repel incoming Li ions from the pointy regions, and accordingly cause the Li ions to be deposited more preferentially on the adjacent area of the pointy regions. Thus, this deposition mechanism suppresses the rapid growth of the pointy regions of the lithium dendrite and leads to a relatively uniform formation of the dendrite. The anions clustered near the dendrite structure lower the local potential of the regions for dendrite candidates, and accordingly, this mechanism enhances the inhibition of the dendrite growth.

Symmetric ions with $d_+ = d_-$

We first illustrate the electric potential map for 1 % salt concentration with no dendrite formation in Fig. 8. When the dielectric constant is high (Fig. 8a), the color gradually becomes brighter from the anode to the cathode, indicating a moderate change in the electric potential between the cathode and anode. The cations (blue) and anions (yellowish-green) are isolated from each other. However, ion pairing and ion clustering occur as the dielectric constant decreases to ε = 20 (Fig. 8b). The spatial changes in the color gradation between the cathode and anode becomes relatively more inhomogeneous. These preliminary results suggest that both the ion aggregation and the resultant spatial inhomogeneity of the electric potential may become critical in considering the dendrite growth.

We now consider the dendrite formation (Fig. 9). In Fig. 9a and Fig. 9b, the black line indicates that the addition of tiny amounts of salt ions (≤5 %) causes significant decreases in the aspect ratio and average height $\langle H \rangle$. However, the changes in both the aspect ratio and average height $\langle H \rangle$ with increasing salt concentration vary non-monotonically, and thus there appear to be optimal values of salt concentration to maximize the uniformity of the dendrite shape and to inhibit the dendrite growth. Here, we attribute the rise from the local minima around 2 % of the volume fraction to increases in the number of ion pairs that do not participate in electrostatic shielding. Moreover, to consider the significance of the electrostatic interactions for dendrite growth relative to that of the excluded volume interactions, we eliminate the ionic charges on the salt ions. In other words, for comparison, we replace the salt ions with uncharged particles. However, the addition of the uncharged particles (1) does not substantially decrease the aspect ratio unless the volume fraction exceeds about 50 % (Fig.

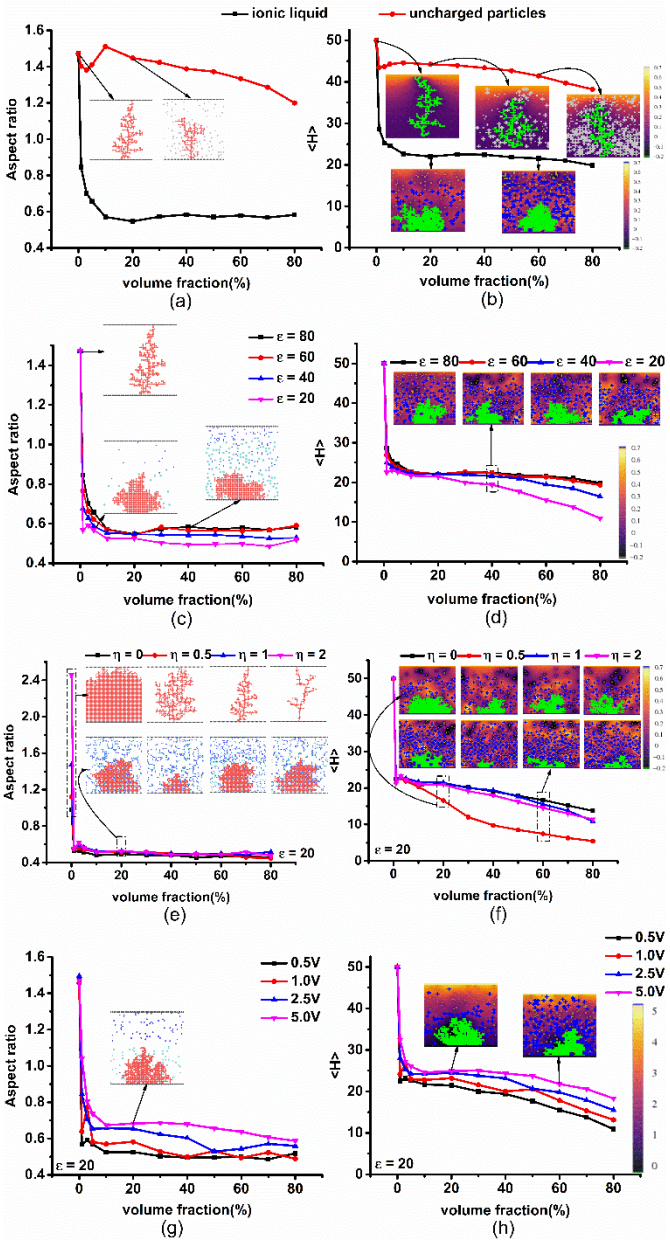

Fig. 11 Effects of the ionic charge, the dielectric constant, the parameter η, and the applied voltage on dendrite growth for the asymmetric ions (d_+:d_-= 2:1). The x-axis is the lattice occupancy of the salts or uncharged particles. $\langle H \rangle$ designates the average height calculated after 2×10^7 MC steps. The applied voltage is 0.5 V in (a) – (f). The dielectric constants are ε = 80, unless otherwise noted. The color classification is the same as that in Fig. 9.

9a) and (2) causes no noteworthy change in the average height $\langle H \rangle$ (Fig. 9b). These results suggest that the large inhibition of dendrite growth arises primarily from the effect of the electrostatic interactions.

Importantly, the salt ions cause the spatial gradient of the electric potential to be more locally inhomogeneous but more globally isotropic than the uncharged counterparts do. This is particularly notable in the regions around the dendrite (see the insets in Fig. 9b) Here, note the basic rule that the tip of the dendrite tends to grow to the brighter regions for the positive, higher electric potential. However, due to the global uniformity of the potential gradient near the dendrite, such a dendritic formation becomes notably more isotropic. Thus, we suggest that this effect facilitates the lateral growth of the dendrite, significantly flattening the dendrite shape.

Next, we consider the effect of the dielectric constant on the dendrite growth (Fig. 9c and Fig. 9d). As in Fig. 9a and Fig. 9b, sharp decreases in the aspect ratio Fig. 9c) and average height (Fig. 9d) from 0 % to 5 % occur. Here, the difference in the

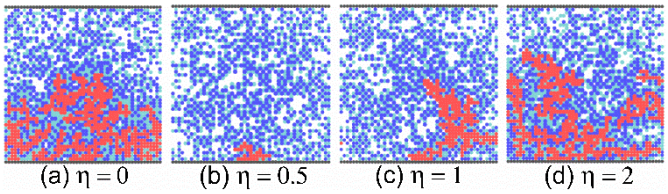

Fig. 10 Snapshots of the dendrite structure with different η values for 60% symmetric ILs and the dielectric constant ε = 20. The light blue and blue points correspond to the cations and anions, respectively.

dielectric constant does not notably change the overall trend of the aspect ratio and the average height when the lattice occupancy of the salt ions is $\lesssim$ 40 %. However, when the volume fraction exceeds about 40 %, the effect of the dielectric constant becomes distinct. It is not entirely clear why decreasing the dielectric constant to ε = 20 causes the local maximum point to shift to the region at the lower salt concentration. Nevertheless, the potential map in the inset shows that the dendrite in the electrolyte with ε = 20 is surrounded by the black regions that indicate that the electric potential is lower than that of the anode. Thus, as indicated by Eq. (5), these negative potential spots appear to inhibit the dendrite growth.

Fig. 9e and Fig. 9f show the effect of the model parameter η in Eq. (5) on the dendrite growth. The average height (Fig. 9f) is significantly affected by the η value, whereas the changes in aspect ratios are relatively insignificant. Moreover, the difference in the trend of the average height among the lines (Fig. 9f) changes non-monotonically. That is, the results change as “black” → “red” → “blue” → “purple” when increasing the η value from 0 to 2. Fig. 9f also indicates that the decrease in the average height when increasing the salt concentration is monotonic when η = 0.5. Thus, in terms of the Li-ion battery design, we do not need to be concerned about the optimal salt concentration that maximally inhibits the dendrite growth.

Fig. 10 illustrates the significance of the value η for the dendrite growth at 60 % salt concentration. The results also suggest that it is important to evaluate the η value [or the accurate form of the probability in Eq. (5)] using more atomistic models that account for the probability of dendrite deposition.

In Fig. 9g and Fig. 9h, we change the applied voltage from 0.5 V to 5.0 V. In the case of large voltages such as 5.0 V, we observed the charge separation between the conducting plates, as illustrated by the inset of Fig. 9g. The overall trends of both the aspect ratio and average height remain similar when the applied voltage is changed. However, notable non-monotonic variations in these values occur when the salt concentration exceeds about 40 %. Accordingly, 0.5 V becomes the optimal operating voltage to inhibit the average height.

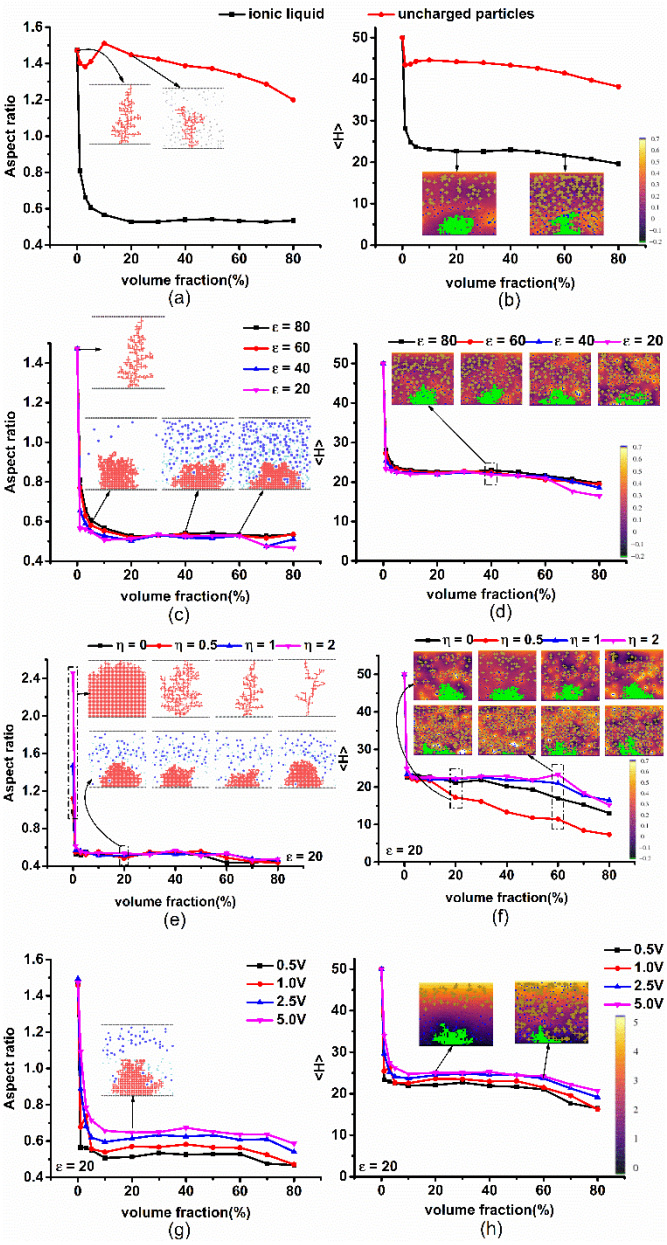

Fig. 12 Effects of the ionic charge, the dielectric constant, the parameter η, and the applied voltage on dendrite growth for the asymmetric ions (d_+:d_-= 1:2). The x-axis is the lattice occupancy of the salts or uncharged particles. $\langle H \rangle$ designates the average height calculated after 2×10^7 MC steps. The applied voltage is 0.5 V in (a) – (f). The dielectric constants are ε = 80, unless otherwise noted. The color classification is the same as that in Fig. 9.

In Fig. 9i-l, we also consider relatively larger symmetric ions and their uncharged counterparts with d = 4 Å to study the size effect. These large ions also mimic an IL. Interestingly, unlike the result in Fig. 9b, the larger uncharged particles promote the dendrite inhibition (Fig. 9j), probably due to the larger excluded volume. Nevertheless, the ions more significantly inhibit the dendrite growth. Moreover, unlike the result in Fig. 9b, the inhibition trend is nearly monotonic. Therefore, ILs would be more tractable in designing Li-ion batteries.

Note that changes in the η cause substantial differences in the aspect ratio and average height (Fig. 9k and Fig. 9l). As in the case of Fig. 9f, η = 0.5 gives rise to a significant inhibition of the average height, and the inhibition effect is even more significant. Note that the overall trends of the aspect ratio and average height are the same among the different η values. Thus, we suggest that a choice of the η value does not alter our conclusion obtained in the present study.

To conclude this subsection, we briefly summarize the mechanism of the dendrite growth with the symmetric small ions as follows: (1) Small amounts of salt ions enhance electrostatic shielding near the dendrite and particularly its pointy regions, and accordingly the dendrite growth is significantly inhibited. (2) Increasing the salt concentration enhances ion clustering, and such ionic aggregates reduce the number of ions that participate in electrostatic shielding. Accordingly, ion clustering weakens the driving force for the inhibition of the dendrite growth until a very high salt concentration such as 80 % is reached. Our results and simulation animation suggest that when the salt concentration is very high, small ion clusters tend to aggregate and to form larger clusters, coherently moving over the entire system. These ions do not tightly bind to each other, and the ion clusters do not live as independent charge-neutral objects. Such large clusters widely cover the dendrite surface and yield the effect of electrostatic shielding. (3) Alternatively, the large ions that mimic ILs significantly inhibit ion clustering, and this effect continues to inhibit the dendrite growth more significantly than the small ions do. This result would probably rationalize the remarkably uniform, unconventional dendrite growth observed in our experiment in Fig. S1†. Nevertheless, the current observation is on the macroscopic scale, whereas our simulation is on the nanometer scale. Thus, further study to bridge the gap between the length scales is required.

Asymmetric ions with $d_+ = 2d_-$

In this subsection, we demonstrate that the size asymmetry between the cation and anion can be critical to inhibit the dendrite growth. We consider the cation and anion diameters to be 4 Å and 2 Å, respectively.

Both the aspect ratio (Fig. 11a) and average height (Fig. 11b) decrease upon the addition of small amounts of salt ions. However, unlike the symmetric uncharged particles in Fig. 9a, the aspect ratio does not notably change even when the salt concentration is as high as 80%. Importantly, these variations are monotonically decreasing and nearly reach plateaus. Thus, we do not need to be concerned about identifying the optimal salt concentration to inhibit the dendrite growth. The inhibition trend for the asymmetric ions is relatively simpler to control than for the small symmetric ions. Here, we observed in the snapshots that ion pairing and clustering are relatively weakened, probably because the cations are large. Thus, we attribute the observed plateaus in the aspect ratio and average height to this size effect.

In contrast to the results in Fig. 9, we observed nearly monotonically decreasing functions in Fig. 11c-h. The results are almost unchanged compared to the changes in the dielectric constant, the model parameter η, and the applied voltage, except for Fig. 11g. As in the case of the symmetric ions (Fig. 9),

Table 1 Training, validation, and test errors of different ENNs. The MAPE is shown in parentheses.

#sub-NNs (ID number)	Topology	Activation Functions in the sub-NN	Training Error	Validation Error	Test Error
8 (1)	4-32-32-2	relu-X-relu, X=sine, cosine, sigmoid, gaussian	13.582 (25.6%)	13.646 (24.8%)	15.323 (29.4%)
8 (2)	4-32-32-2	relu-X-relu, X=relu, cosine, sigmoid, gaussian	13.593 (24.6%)	13.965 (24.2%)	14.959 (28.8%)
8 (3)	4-32-32-2	relu-X-relu, X=sine, tanh, sigmoid, gaussian	13.356 (24.7%)	13.348 (23.9%)	14.998 (29.0%)
8 (4)	4-32-32-2	relu-X-relu, X=sine, relu, sigmoid, gaussian	13.573 (25.5%)	13.863 (26.0%)	14.823 (29.0%)

Table 2 Training, validation, and test errors of the sub-NNs in No.4 ENN. The MAPE is shown in parentheses.

Sub-NN (No.4)	Topology	Activation Functions	Training Error	Validation Error	Test Error
1	4-32-32-2	relu-X-relu, X = sine	506.762 (60.8%)	486.218 (60.8%)	495.212 (61.0%)
2	4-32-32-2	relu-X-relu, X = sine	506.761 (59.9%)	486.217 (60.0%)	495.210 (60.2%)
3	4-32-32-2	relu-X-relu, X = relu	507.018 (100%)	486.466 (100%)	495.465 (100%)
4	4-32-32-2	relu-X-relu, X = relu	17.232 (25.0%)	18.275 (26.9%)	18.838 (27.7%)
5	4-32-32-2	relu-X-relu, X = sigmoid	14.942 (26.0%)	15.282 (28.0%)	16.785 (28.9%)
6	4-32-32-2	relu-X-relu, X = sigmoid	14.520 (24.0%)	15.728 (25.8%)	16.814 (26.7%)
7	4-32-32-2	relu-X-relu, X = Gaussian	15.175 (23.9%)	15.658 (25.9%)	17.162 (26.6%)
8	4-32-32-2	relu-X-relu, X = Gaussian	15.528 (25.2%)	15.524 (26.8%)	17.186 (27.5%)

the decrease in the average height is maximized when η = 0.5 (Fig. 11f). Specifically, unlike the symmetric ions, the effect of the applied voltage on the average height $\langle H \rangle$ is relatively insignificant over nearly the entire salt concentrations (Fig. 11h). These results also suggest that the inhibition of dendrite growth can be relatively easier when the cation size is large enough to weaken ion pairing and clustering. Probably due to this fact, ILs would serve as a good substance to substantially inhibit and flatten the dendrite growth.

Asymmetric ions with $2d_+ = d_-$

Finally, we consider the cation and anion diameters to be 2 Å and 4 Å, respectively. The overall trends of the results in Fig. 12 are very similar to those in Fig. 11. Nevertheless, unlike the results in Fig. 11, the effect of the dielectric constant on the aspect ratio and average height $\langle H \rangle$ becomes insignificant (Fig. 12c and Fig. 12d). Moreover, the increase in the voltage slightly increases the dendrite growth (Fig. 12g and Fig. 12h). Thus, we suggest from the strong similarity between Fig. 11 and Fig. 12 that a critical factor to inhibit dendrite growth is not to change the type of the size asymmetry in ILs, but instead, to decline ion pairing and clustering.

Ensemble neural networks for symmetric ions with $d_+ = d_-$

Finally, we construct a surrogate model that accounts for the lithium dendrite growth via training datasets derived from the MC simulations. We use the dielectric constant ε, the model parameter η, the voltage V, and the volume fraction ϕ for the input and set the aspect ratio and the average height in the output layer. In the present study, one hidden layer is not sufficient to capture the training datasets, especially for the non-monotonic trend of the results, but two hidden layers are adequate. From the calculation of the MSE, we also empirically found that the sub-NN with 32 neurons per hidden layer serves as a good architecture.

Table 1 and Table 2 show the architectures of our ENNs and sub-NNs, respectively, with their training, validation, and test errors. We trained 4 ENNs with different activation functions (Table 1). Table 2 shows the architecture of sub-NNs of No.4 ENN in Table 1 as an example. Here, the chance of overfitting tends to decrease as the difference between the training error and validation error is decreased. Note that some sub-NNs are poorly trained with an error of about 500, yet the corresponding ENN outperforms any sub-NNs and thus provides a good prediction with relatively small errors. Thus, the ENNs can efficiently avoid the local minimum in the MSE that is more likely to occur in a single NN. Despite the large MSE

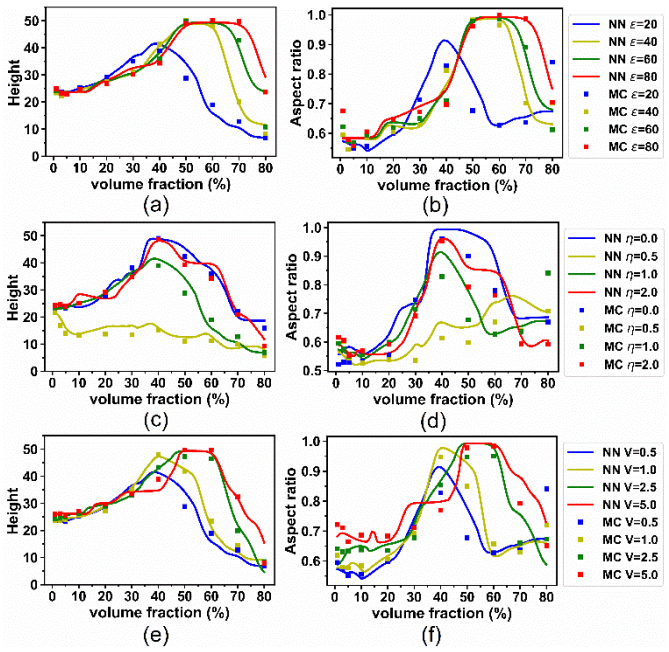

Fig. 13 Comparison between the MC simulation and No.5 sub-NN in Table 2 for the average height and the aspect ratio. The solid lines indicate the prediction from the sub-NN in the range of 1% to 80% volume fraction of salts. The squares indicate the statistical averages calculated from the same datasets of the MC simulations as those used in Fig. 9c-h.

values, the sub-NNs with the sine functions are essential to capture the non-monotonic feature of the simulation results. Such a large MSE value is tamed when incorporated into the ENN.

The MSE is a standard error when evaluating NNs' performance, but relative errors can also serve as a measure to analyze the performance. Thus, we also provide the mean absolute percentage error (MAPE) $\frac{100\%}{n}\sum\left|\frac{y-\hat{y}}{\hat{y}}\right|$ in the tables. No. 1 and No. 2 sub NNs in Table 2 include large errors, yet their relative errors are smaller than 100%. The relative errors appear to be large because the training data for each volume fraction consists of only 20 samples and includes large statistical fluctuation. Here, we remark that reducing the relative error instead of the absolute error may cause significant inconsistency between the qualitative features of the predicted and targeted data. Thus, in this study, the relative error should be viewed as a measure to consider how efficiently the ENNs can predict the "true" statistical average out of noisy information.

We plotted the predicted average heights and the aspect ratio of lithium dendrites in Fig. 13 and Fig. 14. In Fig. 13, we compared the MC simulation result with one of the excellent sub-NNs (No.5 sub-NN in Table 2) containing the sigmoid function for the activation function in the second layer. Note that we used only 20 samples for each volume fraction (i.e., each data point in the figures) to train each sub-NN. Still, our ENNs can reasonably capture and predict the non-monotonic trend of both the average height and the aspect ratio. Fig. 14 shows the comparison between the MC simulation result with the prediction from No. 4 ENN in Table 1. Other ENNs also provide similar consistencies between the MC simulation and ENN prediction. Although some sub-NNs may have large errors, their combination with good sub-NNs tends to provide a robust, relatively accurate ENN. Overall, we suggest that although a single NN can be employed as a surrogate model for the MC simulations, the ENNs are not sensitive to initial weights and are robust against the choice of the activation functions, compared to a single NN.

IV. Summary and Conclusion

We have developed the DLA model proposed by Niemeyer [57] and later developed for zinc dendrite growth by Chen and Jorné [50]. The present study was also motivated by our recent experimental observation regarding remarkably uniform, unconventional lithium dendrite growth in Fig. S1†. Despite the simple algorithm of the growth patterns, the original toy model accounts for the fractal dimensions observed for dielectric breakdown and zinc dendrite. In other words, the model contains an adjustable parameter that controls the growth probability, but it can be fixed when the fractal dimension is determined in experiments. The present study relies on the strong applicability of the model to the pattern formation due to the electrostatic fields. Thus, we applied the algorithm of the pattern formation to metal dendrite growth in salt-containing liquids between the conducting plates. The main conclusion in our study is summarized as follows: (1) The addition of salt ions can significantly flatten the dendrite shape and inhibit the dendrite growth, primarily due to electrostatic shielding near

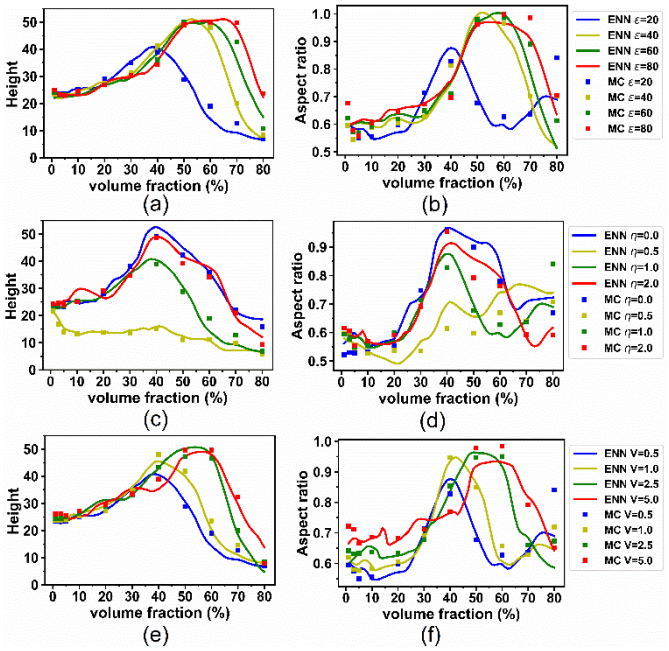

Fig. 14 Comparison between the MC simulation and ENN prediction for the average height and the aspect ratio. The symbols and lines are defined as in Fig. 13.

the pointy regions of the dendrite. (2) It is critical to weaken ion pairing and clustering in electrolytes to inhibit the dendrite growth. Our results show that small salt ions appear to have difficulty achieving this requirement and lead to the undesirable non-monotonic behavior of the dendrite growth as a function of the salt concentration. However, large salts such as ILs can be dissociated near the operating temperatures to a great degree to solve this issue. (3) The size asymmetry that occurs when either the cation or the anion is large (4 Å or larger) affects the dendrite's shape and growth, primarily because ion pairing and clustering are significantly inhibited. In this case, the inhibition of the dendrite growth is not significantly affected by changes in the dielectric constant and applied voltage. The overall conclusion from (1) to (3) remains unchanged when $0 \leq \eta \leq 2$, and appears to hold true in general. Thus, we suggest that ILs be a prospective material to inhibit metal dendrite formation. Among others, the present simulations suggest that ILs with large size asymmetry between the cation and anion serve as a good electrolyte in lithium-ion batteries, as consistent with our experimental observation for lithium deposits under 1M LiPF6 in EC/DMC + 10% [BMIM][TFSI] in ESI†. Concomitantly, the 2D growth appears to be more constrained than the 3D growth. In the case of a 3D model, the dendrite growth in the new lateral direction may easily occur when the ions inhibit the longitudinal growth of the dendrite toward the cathode. Still, this lateral growth appears to facilitate the uniformity of the dendrite surface. Thus, we anticipate that our overall conclusion remains unchanged even in a 3D model.

Finally, we considered a surrogate model that accounts for the MC simulations using ENNs. In our study, we found that a single NN can be consistent with the MC simulation results, but ENNs with sub-NNs can be more robust against the choice of the activation functions and can easily be trained from various initial weights. This is mainly because the ENNs can be trained well when poor sub-NNs are combined with good sub-NNs.

Importantly, unlike 200 samples for the average of the MC simulation results for each volume fraction (i.e., each data point), we used only 20 samples for training. Thus, our surrogate model serves as an alternative to the computationally demanding MC simulations.

Conflicts of interest

There are no conflicts to declare.

Acknowledgements

We are grateful to the High-Performance Computing Shared Facility, Superior, at Michigan Technological University for their essential support. This material is derived from work supported by the Faculty Early Career Development Program of the National Science Foundation under DMR-1944211 and the Research Excellence Fund of Michigan Technological University under REF-01634. R. Shahbazian-Yassar acknowledges the financial support from National Science Foundation CBET-1805938.

References

1. A. Hagopian, M.-L. Doublet and J.-S. Filhol, *Energ Environ Sci*, 2020, **13**, 5186-5197.
2. W.-S. Kim and W.-Y. Yoon, *Electrochimica Acta*, 2004, **50**, 541-545.
3. J.-i. Yamaki, S.-i. Tobishima, K. Hayashi, S. Keiichi, Y. Nemoto and M. Arakawa, *Journal of Power Sources*, 1998, **74**, 219-227.
4. K. Xu, *Chemical Reviews*, 2004, **104**, 4303-4417.
5. Y. Liu, Q. Liu, L. Xin, Y. Liu, F. Yang, E. A. Stach and J. Xie, *Nat Energy*, 2017, **2**, 17083.
6. M. Rosso, C. Brissot, A. Teyssot, M. Dollé, L. Sannier, J.-M. Tarascon, R. Bouchet and S. Lascaud, *Electrochimica Acta*, 2006, **51**, 5334-5340.
7. X. Meng, Y. Xu, H. Cao, X. Lin, P. Ning, Y. Zhang, Y. G. Garcia and Z. Sun, *Green Energy & Environment*, 2020, **5**, 22-36.
8. M. Armand, F. Endres, D. R. MacFarlane, H. Ohno and B. Scrosati, *Nature Materials*, 2009, **8**, 621-629.
9. K. K. Maniam and S. Paul, 2020, **10**, 5321.
10. M. Matsui, *Journal of Power Sources*, 2011, **196**, 7048-7055.
11. C. B. Bucur, T. Gregory, A. G. Oliver and J. Muldoon, *J Phys Chem Lett*, 2015, **6**, 3578-3591.
12. J. Song, H. Lee, M. J. Choo, J. K. Park and H. T. Kim, *Sci Rep-Uk*, 2015, **5**.
13. J. F. Parker, C. N. Chervin, I. R. Pala, M. Machler, M. F. Burz, J. W. Long and D. R. Rolison, *Science*, 2017, **356**, 414-417.
14. R. Selim and P. Bro, *J Electrochem Soc*, 1974, **121**, 1457-1459.
15. P. C. Howlett, D. R. MacFarlane and A. F. Hollenkamp, *Electrochemical and Solid-State Letters*, 2004, **7**, A97.
16. C. Monroe and J. Newman, *J Electrochem Soc*, 2005, **152**, A396-A404.
17. D. T. Hallinan, S. A. Mullin, G. M. Stone and N. P. Balsara, *J Electrochem Soc*, 2013, **160**, A464-A470.
18. S. Choudhury, R. Mangal, A. Agrawal and L. A. Archer, *Nature Communications*, 2015, **6**.
19. W. Y. Li, H. B. Yao, K. Yan, G. Y. Zheng, Z. Liang, Y. M. Chiang and Y. Cui, *Nature Communications*, 2015, **6**.
20. N. S. Schauser, K. J. Harry, D. Y. Parkinson, H. Watanabe and N. P. Balsara, *J Electrochem Soc*, 2015, **162**, A398-A405.
21. J. W. Tan, A. M. Tartakovsky, K. Ferris and E. M. Ryan, *J Electrochem Soc*, 2016, **163**, A318-A327.
22. P. Arora and Z. M. Zhang, *Chemical Reviews*, 2004, **104**, 4419-4462.
23. H. Wu, D. Zhuo, D. S. Kong and Y. Cui, *Nature Communications*, 2014, **5**.
24. C. Monroe and J. Newman, *J Electrochem Soc*, 2003, **150**, A1377-A1384.
25. M. Z. Mayers, J. W. Kaminski and T. F. Miller, *Journal of Physical Chemistry C*, 2012, **116**, 26214-26221.
26. A. Aryanfar, D. Brooks, B. V. Merinov, W. A. Goddard, A. J. Colussi and M. R. Hoffmann, *The Journal of Physical Chemistry Letters*, 2014, **5**, 1721-1726.
27. A. P. Abbott and K. J. McKenzie, *Physical Chemistry Chemical Physics*, 2006, **8**, 4265-4279.
28. A. Basile, A. I. Bhatt and A. P. O'Mullane, *Nature Communications*, 2016, **7**.
29. A. K. Pearson, P. Kao, A. P. O'Mullane and A. I. Bhatt, *Physical Chemistry Chemical Physics*, 2017, **19**, 14745-14760.
30. K. Momeni, Y. Ji, Y. Wang, S. Paul, S. Neshani, D. E. Yilmaz, Y. K. Shin, D. Zhang, J.-W. Jiang, H. S. Park, S. Sinnott, A. van Duin, V. Crespi and L.-Q. Chen, *npj Computational Materials*, 2020, **6**, 22.
31. T. P. Schulze, *Physical Review E*, 2008, **78**.
32. T. R. Krumwiede and T. P. Schulze, *Modelling and Simulation in Materials Science and Engineering*, 2017, **25**.
33. L. A. Selis and J. M. Seminario, *Rsc Advances*, 2019, **9**, 27835-27848.
34. A. A. Wheeler, B. T. Murray and R. J. Schaefer, *Physica D*, 1993, **66**, 243-262.
35. A. Karma and W. J. Rappel, *Physical Review E*, 1998, **57**, 4323-4349.
36. W. J. Boettinger, J. A. Warren, C. Beckermann and A. Karma, *Annu Rev Mater Res*, 2002, **32**, 163-194.
37. L. Q. Chen, *Annu Rev Mater Res*, 2002, **32**, 113-140.
38. Y. Shibuta, Y. Okajima and T. Suzuki, *Science and Technology of Advanced Materials*, 2007, **8**, 511-518.
39. R. S. Qin and H. K. Bhadeshia, *Materials Science and Technology*, 2010, **26**, 803-811.
40. L. Y. Liang, Y. Qi, F. Xue, S. Bhattacharya, S. J. Harris and L. Q. Chen, *Physical Review E*, 2012, **86**.
41. D. R. Ely, A. Jana and R. E. Garcia, *Journal of Power Sources*, 2014, **272**, 581-594.
42. L. Y. Liang and L. Q. Chen, *Appl Phys Lett*, 2014, **105**.
43. L. Chen, H. W. Zhang, L. Y. Liang, Z. Liu, Y. Qi, P. Lu, J. Chen and L. Q. Chen, *Journal of Power Sources*, 2015, **300**, 376-385.
44. D. A. Cogswell, *Physical Review E*, 2015, **92**.
45. A. Jana, D. R. Ely and R. E. García, *Journal of Power Sources*, 2015, **275**, 912-921.
46. K. L. Wang, P. C. Pei, Z. Ma, H. C. Chen, H. C. Xu, D. F. Chen and X. Z. Wang, *J Mater Chem A*, 2015, **3**, 22648-22655.
47. T. Foroozan, F. A. Soto, V. Yurkiv, S. Sharifi-Asl, R. Deivanayagam, Z. Huang, R. Rojaee, F. Mashayek, P. B. Balbuena and R. Shahbazian-Yassar, 2018, **28**, 1705917.
48. V. Yurkiv, T. Foroozan, A. Ramasubramanian, R. Shahbazian-Yassar and F. Mashayek, *Electrochimica Acta*, 2018, **265**, 609-619.
49. V. Yurkiv, T. Foroozan, A. Ramasubramanian, R. Shahbazian-Yassar and F. Mashayek, *MRS Communications*, 2018, **8**, 1285-1291.
50. C. P. Chen and J. Jorne, *J Electrochem Soc*, 1990, **137**, 2047-2051.

51. H. Gould, J. Tobochnik and W. Christian, *An introduction to computer simulation methods : applications to physical systems*, Pearson Addison Wesley, San Francisco, 3rd edn., 2007.
52. S. Wolfram, *Nature*, 1984, **311**, 419-424.
53. M. Kardar, G. Parisi and Y.-C. Zhang, *Physical Review Letters*, 1986, **56**, 889-892.
54. A. Brú, J. M. Pastor, I. Fernaud, I. Brú, S. Melle and C. Berenguer, *Physical Review Letters*, 1998, **81**, 4008-4011.
55. A. Brú, S. Albertos, J. Luis Subiza, J. L. García-Asenjo and I. Brú, *Biophysical Journal*, 2003, **85**, 2948-2961.
56. M. Eden, 1961.
57. L. Niemeyer, L. Pietronero and H. J. Wiesmann, *Physical Review Letters*, 1984, **52**, 1033-1036.
58. I. Borukhov, D. Andelman and H. Orland, *Electrochimica Acta*, 2000, **46**, 221-229.
59. B. Wu, S. Han, K. G. Shin and W. Lu, *Journal of Power Sources*, 2018, **395**, 128-136.
60. M. Quartulli, A. Gil, A. M. Florez-Tapia, P. Cereijo, E. Ayerbe and I. G. Olaizola, *Energies*, 2021, **14**.
61. R. T. Clemen, *International Journal of Forecasting*, 1989, **5**, 559-583.
62. D. H. Wolpert, *Neural Networks*, 1992, **5**, 241-259.
63. X. Zhang, J. P. Mesirov and D. L. Waltz, *Journal of Molecular Biology*, 1992, **225**, 1049-1063.
64. P. Meakin, *Fractals, scaling and growth far from equilibrium*, Cambridge university press, 1998.
65. C. Dominkovics and G. Harsányi, 2010.
66. M. Z. Bazant, B. D. Storey and A. A. Kornyshev, *Physical Review Letters*, 2011, **106**, 046102.
67. F. Chollet and others, Keras, 2015 (https://keras.io).
68. R. P. Feynman, R. B. Leighton and M. Sands, *The Feynman Lectures on Physics, Vol. II: The New Millennium Edition: Mainly Electromagnetism and Matter*, Basic Books, 2015.